Model Predictive Thrust Control With Dynamic Flux-Enhancing for Transverse Flux PM Linear Generator in Direct-Drive Wave Energy Converter

Jianlong Yang, *Student Member, IEEE*, Lei Huang, *Member, IEEE*, Hui Yang, *Senior Member, IEEE*, and Minshuo Chen, *Member, IEEE*

***Abstract*—Transverse flux PM linear generator (TF-PMLG) enables a higher power density under low-speed wave characteristics. However, thrust pulsation and magnetic leakage are major issues in these generators. To address the foregoing problems, a hybrid excitation TF-PMLG is proposed. However, it presents significant control challenges due to large phase inductance and non-negligible internal resistance, particularly under conditions of insufficient bus voltage. Additionally, the necessity for electromagnetic thrust to adapt in real time to wave variations further intensifies the demands on the dynamic performance of the control system. To this end, this article proposes a model predictive thrust control (MPTC) strategy based on optimal flux linkage vector selection. It can effectively mitigate thrust fluctuations of the generator in response to wave action. Furthermore, a dynamic flux-enhancing strategy is developed, which can reduce the dependence on bus voltage magnitude, thus increasing the peak thrust of the generator. Finally, simulations and experimental results are provided to validate the effectiveness of the proposed MPTC methods in direct-drive wave energy converter system.**

***Index Terms*—Direct-drive wave energy converter (DDWEC), model predictive thrust control (MPTC), optimal flux linkage, transverse flux PM linear generator (TF-PMLG).**

I. Introduction

WAVE energy possesses a significant advantage in terms of high energy density and low intermittency [1]. In recent years, the extraction of energy from ocean waves has garnered increasing research attentions. However, the current state of maturity and commercialization of wave energy technology remains substantially lower compared to other renewable energy sources, such as wind and solar. This discrepancy can be attributed primarily to the relatively low efficiency of wave energy converter (WEC) systems, coupled with the susceptibility of these devices to damage under extreme wave conditions. Consequently, the levelized cost of electricity generated from wave energy is still high [2]. Therefore, it is a critical challenge to enhance both the efficiency and operational reliability of wave energy conversion systems [3].

Among various power take-off (PTO) configurations, the point absorption direct-drive WEC (DDWEC) that employs a linear generator is regarded as a promising option for precommercial development [4]. However, the inherently low-velocity nature of ocean waves exerts great challenges in enhancing the power density of generators. In a conventional linear generator, the spatial configuration of teeth and grooves inherently leads to competition for the same planar region [5]. In the transverse flux permanent magnet linear generator (TF–PMLG), the plane of the magnetic circuit is oriented perpendicular to the direction of motion. The transverse flux structure realizes the decoupling of electrical and magnetic loads. The thrust of the generator can be enhanced by achieving a higher rate of change in magnetic energy [6]. It enables an increase in the power density improvement at lower secondary motion velocity [7]. Hence, several TF–PMLGs are utilized in WEC systems [8]. However, the magnetic flux leakage and thrust fluctuations in TF–PMLGs are more pronounced compared to traditional generators. In response, a hybrid excitation TF–PMLG (HE–TF–PMLG) is proposed in [9]. The arrangement and dimensions of the permanent magnets are optimized to mitigate thrust fluctuations. In this case, excitation current is applied to enhance the main magnetic circuit. Although overall performance is improved with this configuration, the space for embedded wires has been additionally expanded. The increased inductance introduces a challenge in operational control of the generator.

Numerous energy-absorbing strategies have been proposed [10], which can be generally categorized into feedback-based real-time control [11] and predictive control utilizing future wave information [12]. The control architecture is structured into two primary layers: the upper layer is responsible for calculating the reference value of the PTO force to optimize energy capture, while the lower layer executes the PTO to track this reference value. Many strategies, particularly those based on economic model predictive control [13], remain at the upper level of simulation research due to their significant computational demands. Conversely, conventional complex conjugate control achieves theoretically lower energy absorption compared to advanced predictive control, yet it demonstrates superior

Received 20 August 2025; revised 10 November 2025; accepted 12 December 2025. Date of publication 16 December 2025; date of current version 20 March 2026. This work was supported by the National Natural Science Foundation of China under Grant 41876096. Recommended for publication by Associate Editor S. S. Lee. *(Corresponding author: Lei Huang.)*

The authors are with College of Electrical Engineering, Southeast University, Nanjing 210096, China, and also with the Marine Renewable Energy Engineering Center, Advanced Ocean Institute of Southeast University, Nantong 226010, China (e-mail: jianlong@seu.edu.cn; huanglei@seu.edu.cn; yang.hui@nuaa.edu.cn; chenminshuo@njit.edu.cn).

Color versions of one or more figures in this article are available at https://doi.org/10.1109/TPEL.2025.3644893.

Digital Object Identifier 10.1109/TPEL.2025.3644893

real-time control performance in hardware implementations. The optimal PTO force generated by the upper controller layer may exhibit significant amplitudes, particularly in the presence of large waves. Besides, the fluctuations in generator thrust can greatly affect the stability of the entire system. Consequently, higher demands are placed on the control performance of the generator. Field-oriented control and direct thrust control are currently well-established methods [14], [15]. As processors become increasingly capable, easy-to-implement MPCs are receiving growing attention. Model predictive current control (MPCC) and model predictive thrust control (MPTC) are the two primary methods employed in linear generators [16], [17]. In this case, MPTC is preferred for its superior thrust dynamics compared to MPCC [18], making it more suitable for the real-time variations in electromagnetic force demands during wave power operations. However, since the flux linkage and thrust are variables in different dimensional levels, the weighting factors for each must be considered in the cost function. In [19], a cost function aimed at minimizing thrust pulsations was designed to determine the optimal weight coefficients, inevitably increasing the computational burden. To mitigate the computational effort, the weighting factors are discretized within a feasible domain in [20]. The cost function associated exclusively with the flux linkage have been raised in [21] and [22] to eliminate the weighting factors directly. These control methods typically focus on either the low volatility of the flux linkage under steady-state conditions, or the response performance during sudden load changes. However, the generator operates under cyclic and dynamic conditions within the DDWEC system. The target thrust continuously increases or decreases over time. When the thrust variation becomes significant, the limited dc-bus voltage may cause the expected voltage vector (VV) to exceed the feasible voltage region, i.e., enter the overmodulation range. A common approach in such cases is to reduce the magnitude of the reference VV while keeping its phase unchanged; however, this inevitably compromises dynamic performance [23]. In MPCC [24] and modulated model predictive control (MMPC) [25], several overmodulation optimization strategies have been developed. These geometric methods are employed to select new reference vectors that lie on the boundary of the linear modulation region and thus maximize control authority [26]. Nevertheless, such techniques have not yet been investigated for MPTC in wave energy generators.

The primary contribution of this article is the development of an enhanced MPTC scheme for DDWEC systems. An optimal vector selection strategy is introduced to simultaneously satisfy stringent steady-state and transient performance requirements under wave energy generation conditions. Based on this framework, an overmodulation optimization algorithm is further proposed to improve control performance during large variations in the target flux linkage. Moreover, a dynamic excitation strategy is designed to extend the peak thrust capability of the generator under limited dc-bus voltage, thereby broadening the stable operating range of the DDWEC system.

The rest of this article is organized as follows. Section II presents the modeling of the DDWEC system and the HE-TF-PMLG. Section III introduces the state-of-the-art MPTC, and

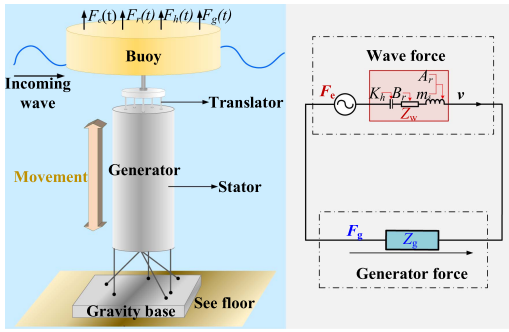

Fig. 1. Schematic diagram of DDWEC.

Section IV details the controller architecture of the proposed improved MPTC scheme. Simulation and experimental validations are provided in Section V. Finally, Section VI concludes this article.

II. Hydrodynamic and Generator Modeling

A. Dynamics Modeling of DDEWC System

The DDWEC system primarily consists of a buoy, a generator, and a gravity block. These three components are interconnected as illustrated in Fig. 1. The generator is actuated by the buoy, which moves up and down in response to the incoming wave. This article focuses exclusively on the heave motion of the device. The force acting on the buoy comprises contributions from both wave and generator.

Based on Cummins' equation, the dynamic model of the system can be alternatively expressed as [27]

$$(m_s+m_\infty)\cdot \mathrm{d}v(t)\mathrm{d}t^{-1}+k_r(t)*v(t)+k_h x(t)=f_e(t)+f_g(t) \tag{1}$$

where the symbol $*$ denotes the convolution operation, m_s is the moving parts mass, $v(t)$ is system heaving velocity, $f_e(t)$ and $f_g(t)$ are the wave excitation and generator forces respectively, k_h denotes the hydrostatic stiffness, $k_r(t)$ represents the radiation impulse response function, and m_∞ is the added-mass at infinite frequency

$$m_\infty = \lim_{\omega\to+\infty} A_r(\omega) \tag{2}$$

where $A_r(\omega)$ is the radiation added-mass, $A_r(\omega)$ and radiation damping $B_r(\omega)$ are defined following Ogilvie's relations [28], and are given by

$$\begin{cases} A_r(\omega) = m_\infty - \omega^{-1}\int_0^{+\infty} k_r(t)\sin(\omega t)dt \\ B_r(\omega) = \int_0^{+\infty} k_r(t)\cos(\omega t)dt \end{cases}. \tag{3}$$

Based on the fundamental principles of Fourier transform theory, (3) leads to the frequency-domain representation of $k_r(t)$

$$K_r(\omega) = B_r(\omega) + j\omega[A_r(\omega) - m_\infty]. \tag{4}$$

Consequently, model (1) can be transformed into the frequency domain as follows:

$$\begin{aligned} &j\omega[m_s + A_r(\omega)]V(\omega) + B_r(\omega)V(\omega) + (j\omega)^{-1}K_h V(\omega) \\ &\quad = F_e(\omega) + F_g(\omega). \end{aligned} \tag{5}$$

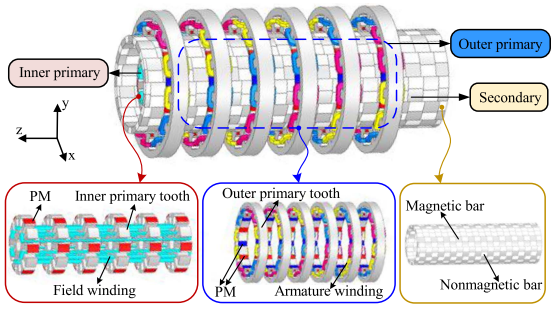

Fig. 2. Topology of HE-TF-PMLG.

TABLE I
MAIN DIMENSION PARAMETERS OF HE-TF-PMLG

Parameter	Value
Outer primary outer diameter	285 mm
Inner primary inner diameter	36 mm
Outer air-gap length	1 mm
Inner air-gap length	1.5 mm
Outer PM thickness	7 mm
Inner PM thickness	3 mm
Number of turns per coil	150

The dynamical model (5) can be expressed with its electrical equivalent as Fig. 1. The excitation force is modeled as an equivalent voltage source, while the corresponding current represents the velocity of device. When the electromagnetic force is synchronized with the velocity, the power flow remains unidirectional from the generator to the load, as:

$$F_g(\omega) = -Z_g(\omega) \cdot V(\omega). \tag{6}$$

Maximum energy extraction is achieved when the output impedance is matched to the internal impedance of the system. Accordingly, the damping coefficient Z_g must fulfill the following condition:

$$Z_g(\omega) = \sqrt{B_r^2(\omega) + [\omega(m_s + A_r(\omega)) - \omega^{-1}K_h]^2}. \tag{7}$$

In simple and efficient control strategies, a characteristic frequency is commonly employed. In most cases, this is selected as the peak frequency of the excitation force. The target generator force in the time domain can be expressed as:

$$f_g^*(t) = -Z_g(\omega_0) \cdot v(t) \tag{8}$$

where ω_0 is the peak frequency and $f_g{}^*(t)$ represents the reference generator force.

B. Machine Mathematical Modelling of HE–TF–PMLG

The configuration of HE–TF–PMLG is shown in Fig. 2. It consists of outer primary, inner primary and secondary between the two primaries. The PMs are placed on both primaries, while the field winding is placed on the inner primary. Alternating rows of magnetic bar and nonmagnetic bar make up the secondary. Misaligned magnetic bar can make the magnetic flux of armature winding change when secondary moves along the z-axis. The dimension parameters of HE-TF-PMLG are given in Table I.

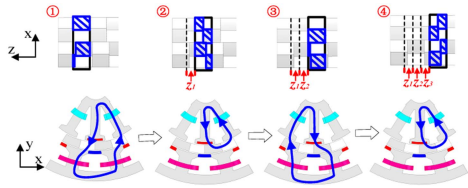

Fig. 3. Magnetic circuit of HE-TF-PMLG.

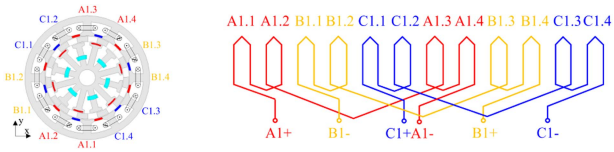

Fig. 4. Coil arrangement and interconnection scheme of a single stator module.

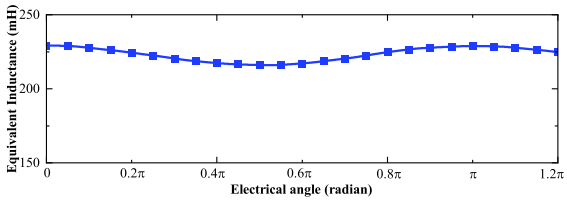

Fig. 5. Equivalent inductance characteristics of HE-TF-PMLG.

The dominated effective flux path of HE-TF-PMLG at typical positions is shown in Fig. 3. The four positions represent the electrical degree at different electrical degrees: 0°; 90°; 180°; and 270°. The flux in the outer primary core is alternating during this motion.

As shown in Fig. 2, the HE-TF-PMLG consists of six stator modules distributed along the z-axis. The coil configuration of a single stator module is illustrated in Fig. 4, where four coils constitute one ABC-phase unit. The six stator modules are connected in series along the z-axis to form the complete three-phase winding system.

The plane of the dominated effective flux is mutually perpendicular to the direction of motion. This transverse flux structure enhances the thrust density. Moreover, the structural parameters are optimized in this generator in order to reduce the inherent effects of magnetic leakage and thrust fluctuations. However, it results in a larger inductance as shown in Fig. 5.

The outer primary voltage and flux linkage equations of HE–TF–PMLG are given by

$$\boldsymbol{u_s} = -R_s \boldsymbol{i_s} + d\boldsymbol{\psi_s} dt^{-1} \tag{9}$$

$$\boldsymbol{\psi_s} = -L_s \boldsymbol{i_s} + \psi_f \tag{10}$$

where $\boldsymbol{u_s}$, $\boldsymbol{i_s}$, ψ_s, are the VV, current vector and flux linkage vector of primary; R_s, L_s are the phase resistance and inductance of armature winding; and ψ_f is the flux linkage vector, consists of excitation flux and PMs flux as

$$\psi_f = \psi_{\rm pm} + M_f i_f \tag{11}$$

where $\psi_{\rm pm}$ is the PMs flux, i_f is the field current, M_f is the mutual inductance between the armature and field winding, and

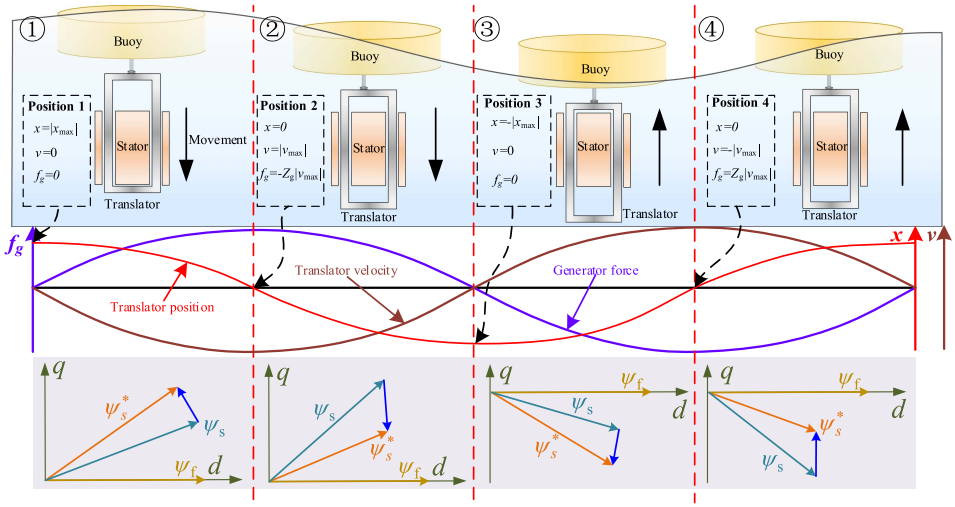

Fig. 6. Working principle of the DDWEC.

the electromagnetic force of the generator can be deduced as

$$f_g = -\frac{3\pi}{2\tau L_s}\boldsymbol{\psi}_s \otimes \psi_f \tag{12}$$

where τ is the pole pitch. In the synchronous rotating d–q reference frame, ψ_{sd} and ψ_{sq} are defined as the component of ψ_s as fellow:

$$\begin{cases} \psi_{sd} = \psi_f - L_d i_d \\ \psi_{sq} = -L_q i_q \\ \psi_s^2 = \psi_{sd}^2 + \psi_{sq}^2 \end{cases} \tag{13}$$

where L_d, L_q, i_d, and i_q are the inductance and current in the synchronous rotating reference frame.

By combining (9)–(11) and (13), the voltage equation can be obtained as

$$\begin{cases} u_d = -R_s i_d - L_d di_d dt^{-1} + \omega_r L_q i_q \\ u_q = -R_s i_q - L_q di_q dt^{-1} + \omega_r(\psi_f - L_d i_d) \\ u_f = R_f i_f + L_f di_f dt^{-1} + M_f di_d dt^{-1} \end{cases} \tag{14}$$

where ω_r is the equivalent electrical angular velocity, $\omega_r = \pi v/\tau$, u_f is the field voltage; and R_f, L_f are the field winding resistance and inductance.

III. New MPTC of PM Linear Machine

The generator is operated under optimal conditions to achieve active power output, while the buoy is driven by ocean waves in a reciprocating motion. The relationship among the ocean wave profile, the translator's position and velocity, and the target generator force over one motion cycle is illustrated in Fig. 5. The translator moves in the negative or positive direction, and the electromagnetic force acts in the opposite direction to resist the motion. When the translator reaches the bottom position, both the thrust and velocity momentarily approach zero, and the polarity of the flux linkage reverses. The variation of ψ_s, ψ_f, and $\psi_s{}^*$ in the d–q plane represents the dynamic modulation process that governs the instantaneous electromagnetic thrust throughout the generating cycle. It is evident that the target thrust increases with the magnitude of the actuator velocity, and vice-versa. Tracking of the target magnetic flux linkage $\psi_s{}^*$ is required when MPTC is employed to achieve the reference value. A new MPTC (NMPTC) method is developed in [22]. NMPTC achieves superior steady-state performance compared to conventional current control and conventional MPTC.

A. Predictive Model

To enable state prediction at the next sampling instant, the continuous-time motor model is discretized. By applying the forward Euler method, (14) are reformulated into a discrete-time representation, yielding the current predictive model:

$$\begin{cases} i_d(k+1) = (1 - R_s T_s L_d^{-1}) i_d(k) \\ \qquad + L_q L_d^{-1} T_s \omega_r(k) i_q(k) - T_s L_d^{-1} u_d(k) \\ i_q(k+1) = (1 - R_s T_s L_q^{-1}) i_q(k) \\ \qquad + L_q^{-1} T_s \omega_r(k)[\psi_f(k) - L_d i_d(k)] - T_s L_d^{-1} u_q(k) \end{cases} \tag{15}$$

where k is the kth instant and T_s is the sampling period, then (13) can be converted into

$$\begin{cases} \psi_{sd}(k+1) = \psi_f(k+1) - L_d i_d(k+1) \\ \psi_{sq}(k+1) = -L_q i_q(k+1) \\ |\boldsymbol{\psi}_s(k+1)| = \sqrt{\psi_{sd}^2(k+1) + \psi_{sq}^2(k+1)} \end{cases}. \tag{16}$$

The employed two-level voltage source rectifier (2L–VSR) can generate eight switching sequences. The corresponding VVs are illustrated in Fig. 7, where u_1 to u_6 represent the six active vectors, and u_0 or u_7 denotes the zero VV.

B. Flux Reference and Cost Function Calculation

The target thrust defined in (8) can be reached through the control of the flux vector. On the basis of the maximum torque current ratio control, the amplitude of the primary flux reference

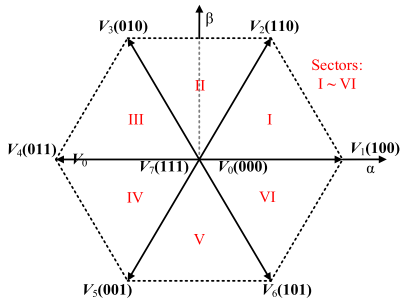

Fig. 7. Basic eight VVs and six sectors for a 2L–VSR.

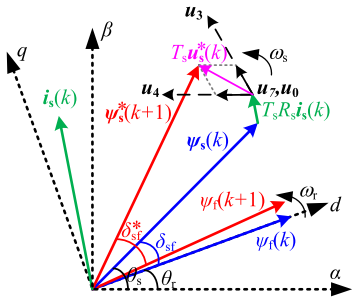

Fig. 8. Relation between different vectors with NMTPC.

is calculated as

$$|\boldsymbol{\psi}_{\mathbf{s}}^*| = \sqrt{\psi_f^2 + \left[2\tau L_q f_g^* \cdot (3\pi\psi_f)^{-1}\right]^2} \tag{17}$$

where $\psi_s{}^*$ is the primary flux reference, the corresponding load angle can thus be calculated as

$$\delta_{sf}^* = \arcsin[2\tau L_q f_g^* \cdot (3\pi\psi_f\,|\psi_s^*|)^{-1}]. \tag{18}$$

The reference primary flux in the *d*–*q* frame can be derived as

$$\begin{cases} \psi_{sd}^*(k+1) = |\boldsymbol{\psi}_{\mathbf{s}}^*(k+1)|\cos\delta_{sf}^* \\ \psi_{sq}^*(k+1) = |\boldsymbol{\psi}_{\mathbf{s}}^*(k+1)|\sin\delta_{sf}^* \end{cases}. \tag{19}$$

The variation of the flux vector in one control period is analyzed as follows. As shown in Fig. 8, $\psi_s(k)$, $\psi_f(k)$, and $\boldsymbol{i}_s(k)$ represent the measurement at the *k*th period. ω_s and ω_r determine the rotational speed of $\psi_{\mathbf{s}}$ and ψ_f, respectively, causing $\theta_s(k)$ and $\theta_r(k)$ to vary with time. The difference between $\theta_s(k)$ and $\theta_r(k)$ is defined as the load angle δ_{sf}. $\boldsymbol{u}_{\mathbf{s}}{}^*(k)$ is the optimal VV applied at the *k*th period, and $\psi_s{}^*(k+1)$ is primary flux reference the at the end of one control period. The mechanical time constant of the system is significantly larger than its electrical counterpart. As a result, the variation in θ_r during one control period is minimal and can be considered negligible compared to θ_s. Then the angle of the VV reference γ in the α–β frame can be obtained as

$$\begin{cases} u_{s\alpha}^* = [\psi_{s\alpha}^*\cos(\theta_r + \delta_{sf}^*) - \psi_{s\alpha}]T_s^{-1} + R_s i_{s\alpha} \\ u_{s\beta}^* = [\psi_{s\beta}^*\sin(\theta_r + \delta_{\mathrm{sf}}^*) - \psi_{s\beta}]T_s^{-1} + R_s i_{s\beta} \end{cases} \tag{20}$$

$$\gamma = \operatorname{acrtan}[u_{s\beta}^* \cdot (u_{s\alpha}^*)^{-1}]. \tag{21}$$

As an illustration, if the optimal VV is determined to be located in Sector III based on the value of γ, three basic VVs (u_3, u_4 and zero VV) are available for selection. When two VVs are used to synthesize the target vector, nine (3×3) basic schemes are available. The dwell time can be obtained as:

$$\begin{cases} t_a = (\boldsymbol{u}_{\mathbf{s}}^* - \boldsymbol{u}_{\mathbf{b}}) \cdot (\boldsymbol{u}_{\mathbf{a}} - \boldsymbol{u}_{\mathbf{b}}) \cdot |\boldsymbol{u}_{\mathbf{a}} - \boldsymbol{u}_{\mathbf{b}}|^{-2} \\ t_b = T_s - t_a \end{cases} \tag{22}$$

where $\boldsymbol{u}_{\mathbf{a}}$ is the first VV, $\boldsymbol{u}_{\mathbf{a}}$=$\boldsymbol{u}_3$, $\boldsymbol{u}_4$, or $\boldsymbol{u}_0(\boldsymbol{u}_7)$, $\boldsymbol{u}_{\mathbf{b}}$ is the second VV, $\boldsymbol{u}_{\mathbf{b}}$=$\boldsymbol{u}_3$, $\boldsymbol{u}_4$, or $\boldsymbol{u}_0(\boldsymbol{u}_7)$, t_a and t_b are the dwell time of $\boldsymbol{u}_{\mathbf{a}}$and $\boldsymbol{u}_{\mathbf{b}}$.

Consequently, a cost function is formulated based solely on the flux values. By combining (15) and (16), the optimal VVs combination is determined through minimization of the cost function as follows:

$$\begin{aligned} C_1 = {} & |\psi_{sd}^*(k+1) - \psi_{sd}(k+1)| \\ & + \left|\psi_{sq}^*(k+1) - \psi_{sq}(k+1)\right|. \end{aligned} \tag{23}$$

IV. Proposed MPTC of HE–TF–PMLG

The HE–TF–PMLG features high thrust and power density, but also exhibits increased internal resistance and inductance. As shown in Fig. 6, the generator thrust typically varies, which imposes higher requirements on both steady-state and transient control performance. In addition, an excessively high peak thrust may lead to insufficient bus voltage, which subsequently results in thrust fluctuations and excursions. To enhance control performance under wave excitation, an improved MTPC (IMPTC) method is proposed in this section.

A. Implement Method for IMPTC

Fig. 9 shows the vector control diagram of IMPTC for generator. Different from NMPTC scheme in Section III, the optimal VV is not computed in advance but is directly regulated based on the variation of the flux vector.

A feasible domain, bounded by the endpoints of the $\psi_{\mathbf{s}}(k)$ and oriented perpendicular to the *d*–axis, is defined as follows:

$$\boldsymbol{W}(k) = \{\boldsymbol{\kappa} \in \mathbb{R}^2 \,|0 \le \boldsymbol{n}_{\mathbf{d}}^{\mathbf{T}}(\boldsymbol{\kappa} - \boldsymbol{\kappa}_{\mathbf{0}}) \le \lambda\Delta f_g^*(k)\} \tag{24}$$

where $\boldsymbol{W}(k)$ is the, κ is any point in the *d*–*q* plane, $\kappa_{\mathbf{0}}$ is the endpoints of the $\psi_s(k)$, $\boldsymbol{n}_{\mathbf{d}}{}^{\boldsymbol{T}}$ is the unit vector perpendicular to the *d*–axis, and $\lambda\Delta f_g{}^*(k)$ defines the width of the feasible domain, $\lambda = 2\tau L_q{\cdot}[3\pi\psi_f(k)]^{-1}$.

The reference thrust increment is fulfilled only when the applied VV terminates at the upper boundary of the defined

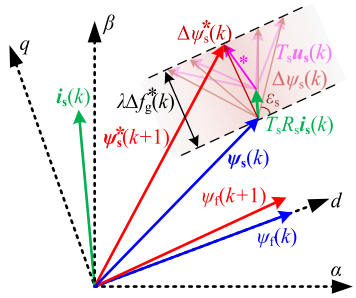

Fig. 9. Relation between different vectors with IMTPC.

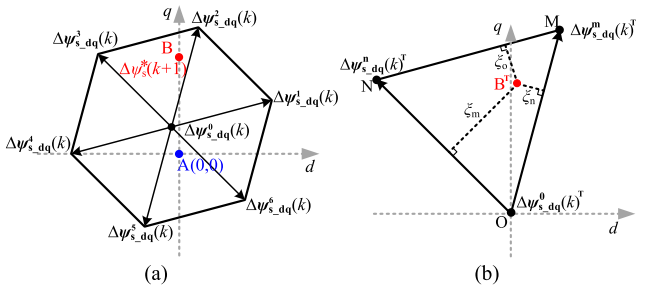

Fig. 10. Vector diagram of primary flux increment. (a) Corresponding hexagonal variation. (b) Vector distributor.

region. The amplitude of the primary flux increment is defined as

$$|\Delta\boldsymbol{\psi}_{\mathbf{s}}(k)| = \Xi(\varepsilon_s) = \lambda\Delta f_g^*(k)\,.\,\sin^{-1}(\varepsilon_s) \tag{25}$$

where ε_s is the angle between $\Delta\psi_s(k)$ and upper boundary, and $\Xi(\varepsilon_s)$ represents a function of the primary flux increment.

To minimize the variation in $\psi_{\mathbf{s}}$, the optimal angle is selected as $\varepsilon_s^*=\pi/2$, then the optimal flux increment satisfies $|\Delta\boldsymbol{\psi}_s^*(k)| = \Xi(\varepsilon_s^*)$. As illustrated in Fig. 9, the corresponding reference primary flux increment in the d–q frame can be obtained as

$$\begin{bmatrix}\Delta\psi_{sd}^*(k)\\ \Delta\psi_{sq}^*(k)\end{bmatrix} = |\boldsymbol{\Delta\psi}_{\mathbf{s}}^*(k)|\begin{bmatrix}\cos\varepsilon_s^*\\ \sin\varepsilon_s^*\end{bmatrix}. \tag{26}$$

By combining (9), (10), and (13), the variation of ψ_s at kth can be expressed in the d–q frame as

$$\begin{bmatrix}\Delta\psi_{sd}(k)\\ \Delta\psi_{sq}(k)\end{bmatrix} = T_s\begin{bmatrix}u_d(k)\\ u_q(k)\end{bmatrix} + \mathbf{G_f}(k)\begin{bmatrix}\psi_{sd}(k)\\ \psi_{sq}(k)\end{bmatrix} + \mathbf{H_f}(k) \tag{27}$$

where

$$\mathbf{G_f}(k) = \begin{bmatrix}-R_sL_d^{-1}T_s & T_s\omega_r(k)\\ -T_s\omega_r(k) & -R_sL_q^{-1}T_s\end{bmatrix}, \mathbf{H_f}(k) = \begin{bmatrix}R_sL_d^{-1}T_s\psi_f(k)\\ 0\end{bmatrix}.$$

A simplified form of (27) can be written as

$$\boldsymbol{\Delta\psi}_{\mathbf{s\_dq}}(k) = T_s\boldsymbol{u}_{\mathbf{dq}}(k) + \mathbf{G_f}(k)\boldsymbol{\psi}_{\mathbf{s\_dq}}(k) + \mathbf{H_f}(k). \tag{28}$$

The corresponding hexagonal variation of the primary flux in Fig. 10(a), can be predicted based on the $\Delta\psi_{\mathbf{s\_dq}}$ induced by each VV within the hexagon in Fig. 7. The point B is the position corresponding to the reference $\Delta\boldsymbol{\psi}_{\mathbf{s\_dq}}^*(k)$. When no active VV is applied, the predicted increment at kth can be expressed as

$$\boldsymbol{\Delta\psi}_{\mathbf{s\_dq}}^{\mathbf{0}}(k) = \mathbf{G_f}(k)\boldsymbol{\psi}_{\mathbf{s\_dq}}(k) + \mathbf{H_f}(k) \tag{29}$$

where $\Delta\boldsymbol{\psi}_{\mathbf{s\_dq}}^{\mathbf{0}}(k)$ denotes the increment under zero VVs ($\boldsymbol{u_0}$, $\boldsymbol{u_7}$). Based on (28), the increment under the active VV is able to be predicted by

$$\begin{cases}\boldsymbol{\Delta\psi}_{\mathbf{s\_dq}}^{\boldsymbol{i}}(k) = T_s\boldsymbol{u}_{\mathbf{dq}}^{\boldsymbol{i}}(k) + \boldsymbol{\Delta\psi}_{\mathbf{s\_dq}}^{\mathbf{0}}(k)\\ \boldsymbol{\Delta\psi}_{\mathbf{s\_dq}}^{\boldsymbol{j}}(k) = T_s\boldsymbol{u}_{\mathbf{dq}}^{\boldsymbol{j}}(k) + \boldsymbol{\Delta\psi}_{\mathbf{s\_dq}}^{\mathbf{0}}(k)\end{cases} \tag{30}$$

where the $\Delta\boldsymbol{\psi}_{\mathbf{s\_dq}}^{\boldsymbol{i,j}}(k)$ is the primary flux increment under two adjacent VVs $\boldsymbol{u}_{\mathbf{dq}}^{\boldsymbol{i,j}}$ in the sectors I–VI as given in Table II.

TABLE II
APPLIED ADJACENT VVS IN DIFFERENT SECTORS

Sector	I	II	III	IV	V	VI
$\boldsymbol{u}_{\mathbf{dq}}^{\boldsymbol{i}}$	$\boldsymbol{u}_{\mathbf{dq}}^{\mathbf{1}}$	$\boldsymbol{u}_{\mathbf{dq}}^{\mathbf{2}}$	$\boldsymbol{u}_{\mathbf{dq}}^{\mathbf{3}}$	$\boldsymbol{u}_{\mathbf{dq}}^{\mathbf{4}}$	$\boldsymbol{u}_{\mathbf{dq}}^{\mathbf{5}}$	$\boldsymbol{u}_{\mathbf{dq}}^{\mathbf{6}}$
$\boldsymbol{u}_{\mathbf{dq}}^{\boldsymbol{j}}$	$\boldsymbol{u}_{\mathbf{dq}}^{\mathbf{2}}$	$\boldsymbol{u}_{\mathbf{dq}}^{\mathbf{3}}$	$\boldsymbol{u}_{\mathbf{dq}}^{\mathbf{4}}$	$\boldsymbol{u}_{\mathbf{dq}}^{\mathbf{5}}$	$\boldsymbol{u}_{\mathbf{dq}}^{\mathbf{6}}$	$\boldsymbol{u}_{\mathbf{dq}}^{\mathbf{1}}$

To simplify the analysis, $\Delta\boldsymbol{\psi}_{\mathbf{s\_dq}}^{\mathbf{0}}(k)$ is translated to the coordinate origin. The flux increment can then be expressed as

$$\begin{cases}\boldsymbol{\Delta\psi}_{\mathbf{s\_dq}}^{\mathbf{0},\boldsymbol{i},\boldsymbol{j}}(k)^T = \boldsymbol{\Delta\psi}_{\mathbf{s\_dq}}^{\mathbf{0},\boldsymbol{i},\boldsymbol{j}}(k) - \boldsymbol{\Delta\psi}_{\mathbf{s\_dq}}^{\mathbf{0}}(k)\\ \boldsymbol{\Delta\psi}_{\mathbf{s\_dq}}^{*}(k)^T = \boldsymbol{\Delta\psi}_{\mathbf{s\_dq}}^{*}(k) - \boldsymbol{\Delta\psi}_{\mathbf{s\_dq}}^{\mathbf{0}}(k)\end{cases} \tag{31}$$

where $\Delta\boldsymbol{\psi}_{\mathbf{s\_dq}}^{\mathbf{0},\boldsymbol{i},\boldsymbol{j}}(k)^{\mathrm{T}}$ and $\Delta\boldsymbol{\psi}_{\mathbf{s\_dq}}^{*}(k)^T$ corresponds to the converted value of $\Delta\boldsymbol{\psi}_{\mathbf{s\_dq}}^{\mathbf{0},\boldsymbol{i},\boldsymbol{j}}(k)$ and $\Delta\boldsymbol{\psi}_{\mathbf{s\_dq}}^{*}(k)$ after transformation.

The VV combination in the optimal sector can be determined by minimizing the following cost function as

$$\begin{aligned}C_2 = &\left|\Delta\psi_{sd}^*(k)^T - \Delta\psi_{sd}^i(k)^T\right| + \left|\Delta\psi_{sq}^*(k)^T - \Delta\psi_{sq}^i(k)^T\right|\\ &+ \left|\Delta\psi_{sd}^*(k)^T - \Delta\psi_{sd}^j(k)^T\right| + \left|\Delta\psi_{sq}^*(k)^T - \Delta\psi_{sq}^j(k)^T\right|.\end{aligned} \tag{32}$$

Therefore,

$$[\boldsymbol{\Delta\psi}_{\mathbf{s\_dq}}^{\mathbf{m}}(k)^T, \boldsymbol{\Delta\psi}_{\mathbf{s\_dq}}^{\mathbf{n}}(k)^T] = \min C_2(.) \tag{33}$$

where $\Delta\boldsymbol{\psi}_{\mathbf{s\_dq}}^{\mathbf{m}}(k)^T$ and $\Delta\boldsymbol{\psi}_{\mathbf{s\_dq}}^{\mathbf{n}}(k)^T$ is the optimal flux increment as shown in Fig. 10(b).

According to Fig. 10(b), the coordinates of points O, B^{T}, M, and N are given by: O(0, 0); B^T $(\Delta\boldsymbol{\psi}_{\mathbf{sd}}^*(k)^T, \Delta\boldsymbol{\psi}_{\mathbf{sq}}^*(k)^T)$; $\mathrm{M}(\Delta\boldsymbol{\psi}_{\mathbf{sd}}^{\mathbf{m}}(k)^T, \Delta\boldsymbol{\psi}_{\mathbf{sq}}^{\mathbf{m}}(k)^T)$; and $\mathrm{N}(\Delta\boldsymbol{\psi}_{\mathbf{sd}}^{\mathbf{n}}(k)^T, \Delta\boldsymbol{\psi}_{\mathbf{sq}}^{\mathbf{n}}(k)^T)$. The distances from point B to each side of the equilateral triangle $\triangle$OMN can be calculated as follows

$$\begin{cases}\xi_o = \left|\overrightarrow{\mathrm{MN}}\right|^{-1}\,.\,\left|\overrightarrow{\mathrm{MN}}\times\overrightarrow{\mathrm{MB}^T}\right|\\ \xi_m = \left|\overrightarrow{\mathrm{OM}}\right|^{-1}\,.\,\left|\overrightarrow{\mathrm{OM}}\times\overrightarrow{\mathrm{OB}^T}\right|\\ \xi_n = \left|\overrightarrow{\mathrm{ON}}\right|^{-1}\,.\,\left|\overrightarrow{\mathrm{ON}}\times\overrightarrow{\mathrm{OB}^T}\right|\end{cases} \tag{34}$$

where ξ_o, ξ_m, and ξ_n denote the distances from point B^{T} to lines MN, ON, and OM, respectively. In order to determine whether the target vector lies within the overmodulation region, define:

$$\begin{cases}\xi_s = \xi_o + \xi_m + \xi_n\\ \xi_t = \frac{\sqrt{3}}{2}\left|\overrightarrow{\mathrm{MN}}\right|\end{cases}. \tag{35}$$

For the equilateral triangle, the sum of the perpendicular distances from any interior point to its three sides is constant and equal to ξ_t. If this sum ξ_s exceeds ξ_t, the point lies outside the triangle. Therefore, a duty cycle calculation method is proposed

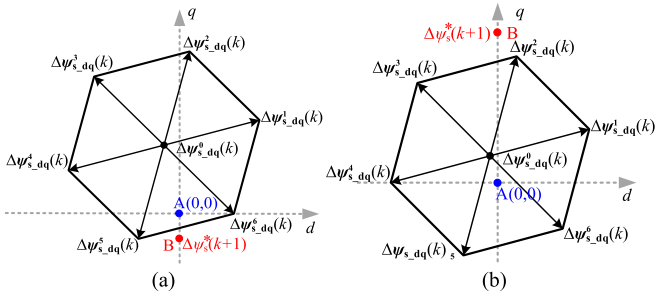

Fig. 11. Target primary flux increment beyond the boundary. (a) Due to high peak thrust. (b) Due to large thrust variation.

as follows:

$$\begin{cases} \text{if } \xi_s = \xi_t: \\ d_m = \xi_m \cdot \xi_s^{-1}, d_n = \xi_n \cdot \xi_s^{-1}, d_o = \xi_o \cdot \xi_s^{-1} \\ \text{if } \xi_s > \xi_t: \\ d_m = \xi_m \cdot (\xi_m + \xi_n)^{-1}, d_n = \xi_n \cdot (\xi_m + \xi_n)^{-1}, d_o = 0 \end{cases} \tag{36}$$

where d_m, d_n, and d_o represent the duty cycles of the $\Delta\boldsymbol{\psi}^{\mathbf{m}}_{\mathbf{s\_dq}}(k)^T$, $\Delta\boldsymbol{\psi}^{\mathbf{n}}_{\mathbf{s\_dq}}(k)^T$ and $\Delta\boldsymbol{\psi}^{\mathbf{0}}_{\mathbf{s\_dq}}(k)^T$.

B. Reference Vector Optimization Under Bus Voltage Constraints

In WEC systems, the dc-bus voltage is typically kept at a moderate level. This is due to the need to balance performance, safety, cost, and control stability. In both grid-connected and stand-alone systems, hybrid energy storage devices are commonly integrated into the dc link to enhance power quality [29]. To ensure system stability, the dc-bus voltage is constrained to fluctuate within a narrow range, and is regulated to remain near a fixed reference over time. In large wave conditions, higher peak thrust is required to sustain continuous power generation. This implies that the primary flux ψ_s remains at a high level during the peak thrust interval. Since the internal resistance of the generator is nonnegligible, insufficient bus voltage may also occur even when the refence primary flux increment $\Delta\psi_s{}^*(k)$ is small. In this case, the target vector lies outside the hexagonal boundary, as illustrated in Fig. 11(a). In adverse wave conditions, the thrust may exhibit abrupt variations. According to (25), the corresponding target increment $\Delta\boldsymbol{\psi}^*_{\mathbf{s}}(k)$ may exceed the boundary due to the large inductance of the generator, as illustrated in Fig. 11(b).

In cases of insufficient bus voltage, a boundary point is often selected as a new reference. The conventional approach, as expressed in (36), first evaluates whether the target vector exceeds the linear modulation limit based on parameter ξ_s. If so, a new reference point—denoted as point C in Fig. 12.—is computed accordingly.

The conventional method of reference vector optimization can enhance voltage utilization. However, it does not account for the flux behavior during dynamic transients, which may lead to certain deviations between the actual and target values. An improved optimization method is adopted, and its underlying principle is illustrated in Fig. 12. The introduced method effectively mitigates magnetic flux trajectory drift in the overmodulation region, thereby ensuring accurate dynamic trajectory tracking and fast transient response. Point A^T represents the pre-transition state, and vector A^TB^T denotes the trajectory of the flux variation toward the target value. The point D, where the trajectory intersects the boundary, is selected as the optimized reference point; that is, the intersection of A^TB^T and line segment MN. The corresponding calculations are given as follows:

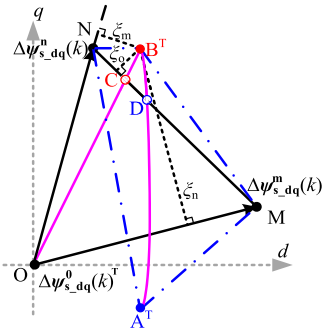

Fig. 12. Geometrical analysis of overmodulation zone.

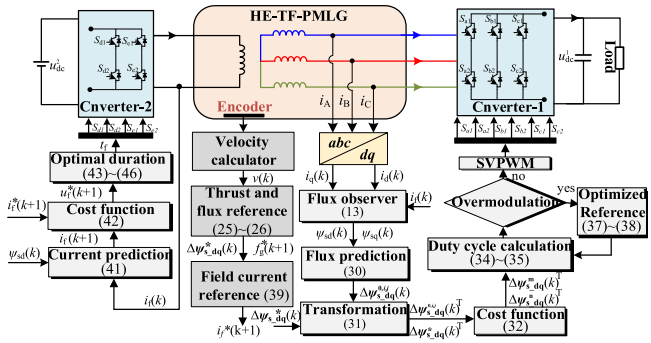

Fig. 13. Overall control block diagram of IMPTC.

$$\begin{bmatrix} \Delta\psi^*_{sd}(k)^T + \Delta\psi^0_{sd}(k) & \Delta\psi^n_{sd}(k)^T - \Delta\psi^m_{sd}(k)^T \\ \Delta\psi^*_{sq}(k)^T + \Delta\psi^0_{sq}(k) & \Delta\psi^n_{sq}(k)^T - \Delta\psi^m_{sq}(k)^T \end{bmatrix} \begin{bmatrix} r_1 \\ r_2 \end{bmatrix} = \begin{bmatrix} \Delta\psi^n_{sd}(k)^T + \Delta\psi^0_{sd}(k) \\ \Delta\psi^n_{sq}(k)^T + \Delta\psi^0_{sq}(k) \end{bmatrix} \tag{37}$$

$$\boldsymbol{\Delta\psi}^*_{\mathbf{s\_dq}}(k)^{\mathrm{D}} = \boldsymbol{\Delta\psi}^*_{\mathbf{s\_dq}}(k)^{\mathrm{T}} + (r_1 - 1) \cdot \boldsymbol{\Delta\psi}^{\mathbf{0}}_{\mathbf{s\_dq}}(k) \tag{38}$$

where the variables r_1 and r_2 serve as intermediate quantities in the computation, $\Delta\boldsymbol{\psi}^*_{\mathbf{s\_dq}}(k)^D$ represents the optimized reference vector.

C. Dynamic Flux-Enhancing Strategy

HE–TF–PMLG contains two excitation sources, with one provided by PMs and the other by electrical excitation. The PMs generate the main flux, while the field current contributes the auxiliary flux. Under severe wave conditions, the field current can be regulated to strengthen the flux. This allows the system to achieve higher peak thrust even under limited bus voltage. The overall control structure is illustrated in Fig. 13, where the

excitation current is independently controlled. Here, i_f and u_f represent the excitation current and excitation voltage, respectively.

In conventional constant flux-enhancing (CFE) strategy, the field current is typically maintained at a constant value for a certain period. Notably, the electromagnetic force in the DDWEC system exhibits a sinusoidal-like variation. The reference excitation current for the next reciprocating cycle is determined by evaluating the average thrust over the current cycle and comparing it with the rated thrust. As the target amplitude of the electromagnetic force decreases, the required excitation current correspondingly diminishes. Consequently, this article proposes a dynamic flux-enhancing (DFE) strategy to enhance adaptability to the operational conditions of wave power generation. In the DFE strategy, the field current is modulated in accordance with the amplitude of the electromagnetic force, leading to a corresponding design of the reference currents as follows:

$$i_f^*(k+1) = \vartheta_f \cdot \left| f_g^*(k+1) \right| \tag{39}$$

where $i_f^*(k+1)$ is the target excitation current at $(k+1)$th, ϑ_f is a constant determined by the ratio between the rated thrust and the rated excitation current, $\vartheta_f = 0.02$.

It should be noted that, under the normal low-velocity and high-thrust operating conditions of the DDWEC, the electrical frequency remains low, and the excitation current mainly functions to enhance the flux. Therefore, the voltage margin constraint is not critical within this range, and the reference excitation current can be directly determined by the amplitude of the electromagnetic force as given in (39). However, when the generator operates under extremely severe sea states and the rotational velocity increases markedly, the influence of electrical frequency on the voltage margin should also be considered. In such cases, the excitation current gradually decreases with increasing electrical frequency to ensure reliable operation, as further described by the extended current distribution model in

$$i_f^*(k+1) = \begin{cases} \vartheta_f \cdot \left| f_g^*(k+1) \right|, & 0 < \omega_r(k+1) \le \omega_{rt} \\ -\vartheta_\omega \cdot \left| \omega_r(k+1) - \omega_{rt} \right| + \vartheta_f \cdot \left| f_g^*(k+1) \right|, & \omega_{rt} < \omega_r(k+1) \le \omega_{rz} \\ 0, & \omega_r(k+1) > \omega_{rz} \end{cases} \tag{40}$$

where ω_{rt} denotes the maximum electrical frequency within the low- velocity operating range $\omega_{rt} = 292$ rad/s; ω_{rz} represents the maximum electrical frequency when the excitation current decreases to zero, $\omega_{rz} = 480$ rad/s; and ϑ_ω is a constant parameter set to 0.0265.

The target field current can be realized by independent control of the dc voltage source. The field current at $(k+1)$th can be predicted as

$$i_f^h(k+1) = L_d C_f T_s u_f^h(k) + M_f C_f \Delta\psi_{sd}^*(k) + (1 - L_d R_f C_f T_s) i_f(k) \tag{41}$$

where $C_f = (L_f L_d + M f^2)^{-1}$, $h = 12$, $u_f^h(k)$ is the nonzero VVs, and $i_f^h(k+1)$ is the predicted field current.

To obtain the optimal vector, the cost function of the field current is given by

$$C_3 = \left[i_f^*(k+1) - i_f(k+1) \right]^2 \tag{42}$$

$$u_f^*(k) = \min C_3(\cdot) \tag{43}$$

where u_f^* is the optimal VV, the ideal voltage reference u_f^{ref} for the excitation felid circuit can likewise be expressed as

$$u_f^{\text{ref}}(k) = \left[i_f^*(k+1) + (L_d R_f C_f T_s - 1) i_f(k+1) - M_f C_f \Delta\psi_{sd}^*(k) \right] \cdot L_d^{-1} C_f^{-1} T_s^{-1}. \tag{44}$$

Additionally, the optimum duration of the excitation voltage is calculated as

$$t_f = T_s u_f^*(k) \cdot u_{\text{f}}^{\text{ref}}(k)^{-1}. \tag{45}$$

Due to the constraints imposed by the bus voltage, there are instances where the optimal duration of the VV either exceeds these limitations or becomes negative. Consequently, the following constraints are established to address this situation as

$$t_f = \begin{cases} 0, t_f \le 0 \\ t_f, 0 < t_f < T_s \\ T_s, t_f \ge T_s \end{cases}. \tag{46}$$

In summary, the system is composed of two independent components: the rectification and field circuit, each capable of being controlled separately. As shown in Fig. 13, the applied controller can be summarized in the following steps.

1) Measure the outer primary current, field current, secondary velocity, and dc-link voltage of rectification and field circuit.
2) Calculate the reference thrust based on the measured values.
3) Calculate the reference primary flux increment and reference field currents based on the reference thrust.
4) Vector transformation and optimize the cost function of flux increment for the optimal sector.
5) Calculate duty cycle and optimized reference.
6) Optimize the cost function of the field current for the optimal VV and optimal duration.
7) Generate the switching pulses.

V. Simulation and Experimental Results

IMPTC is introduced in this article, and an optimized modulation method based on it is presented. For simplicity, the IMPTC methods based on different modulation schemes are designated as IMPTC-1 and IMPTC-2. IMPTC-1 corresponds to the conventional IMPTC method with the overmodulation approach using point C in Fig. 12. IMPTC-2 represents the IMPTC method with the proposed overmodulation option, which uses point D in Fig. 12. To validate the effectiveness of the proposed IMPTC schemes, their performance is compared with that of the NMPTC. Detailed simulations and experiments are carried out

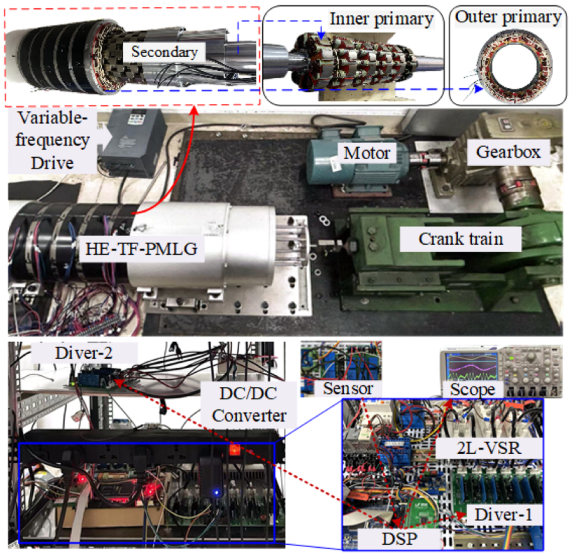

Fig. 14. Experimental platform of system.

TABLE III
APPLIED VVS OF FIELD CURRENT

Sector	Active VV	Zero VV	
I	$u_f^1(01)$	$u_f^0(00)$	$u_f^3(11)$
II	u_f^2 (10)	$u_f^0(00)$	$u_f^3(11)$

in this section. The experimental setup is developed as illustrated in Fig. 14.

It can be noticed from Fig. 14 that the mechanical subsystem mainly consists of a motor, a gearbox, a crank train, and a generator. The motor is supplied by a variable-frequency drive, allowing its speed to be flexibly adjusted. The gearbox converts the high-speed, low-torque output of the motor into low-speed, high-torque motion. This rotational motion is then transformed by the crank train into a linear displacement with a sinusoidal-like velocity profile. In addition, the generator is based on the HE-TF-PMLG. It includes the inner primary, outer primary, and the secondary as shown in the exploded view. Then the linear motion generated by the crank train is transmitted to the secondary mover of the HE-TF-PMLG. A 2L-VSR is employed to convert the three-phase ac output of the generator into dc, which is then fed into the dc link. Meanwhile, a dc/dc converter is employed to supply the field current. At the core of the system, a TMS320F28335 digital signal processor is used to execute the control algorithm in real time. It acquires signals from various sensors, processes the control logic, and generates PWM signals to drive the converters. The parameters of the system are given in Table IV.

It should be emphasized that the present validation is carried out in a laboratory environment, where the excitation motion is generated by a motor–gearbox–crank mechanism instead of ocean waves. Although simplified, this configuration is deliberately designed to provide controllable and repeatable conditions, which are particularly suitable for rigorous evaluation of the proposed control algorithm. Within such a setup, the transient response, steady-state accuracy, and robustness of the control strategy can be thoroughly investigated. To further enhance the reliability of the proposed method, future work will extend the validation to wave-tank experiments and, ultimately, to full-scale sea trials, where the practicability of the proposed approach can be comprehensively demonstrated.

TABLE IV
KEY PARAMETERS OF THE SYSTEM

Parameter	Value
Outer primary resistance/R_s	7.8 Ω
Field resistance/R_f	2.7 Ω
Load resistance/R_d	50 Ω
Permanent magnets flux/Ψ_{pm}	0.139 Wb
d-axis inductance/L_d	216 mH
q-axis inductance/L_q	229 mH
Field winding inductance/L_f	97 mH
Mutual field-armature inductance/M_f	15.8 mH
Pole pitch/τ	15 mm

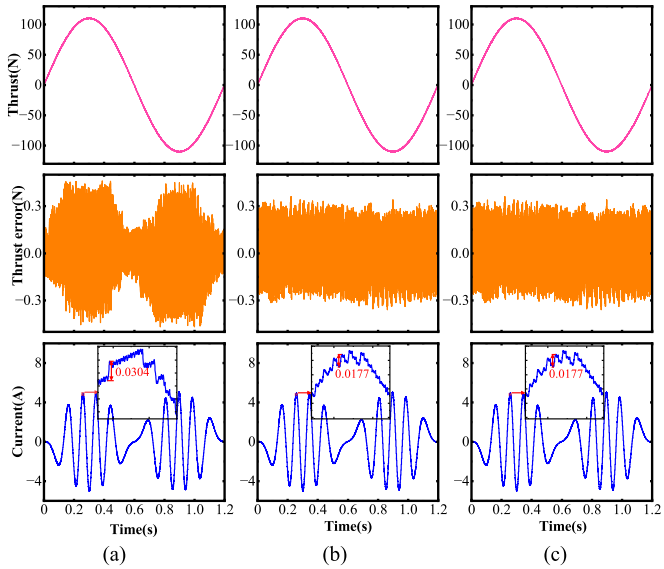

Fig. 15. Simulation results of thrust, thrust error and phase current at a peak thrust of 110 N. (a) NMPTC. (b) IMPTC-1. (c) IMPTC-2.

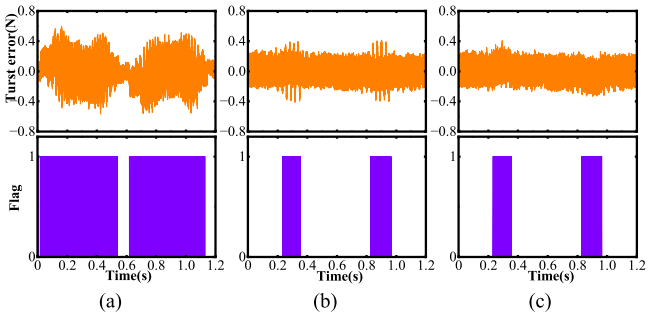

Fig. 16. Simulation results of thrust and Flag at a peak thrust of 130 N. (a) NMPTC. (b) IMPTC-1. (c) IMPTC-2.

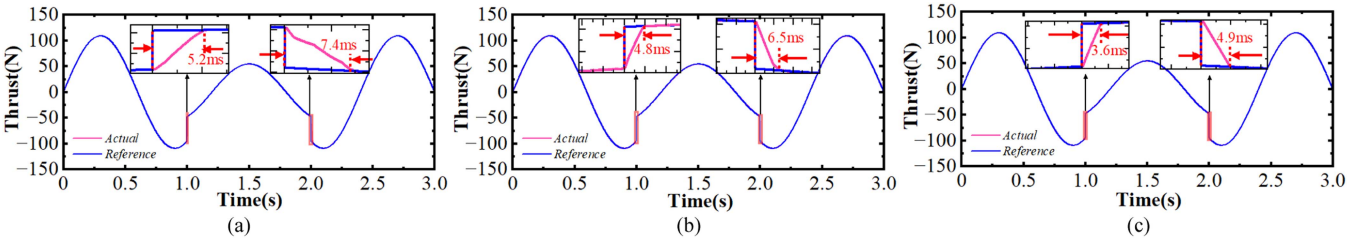

Fig. 17. Dynamic simulation results when the thrust suddenly changes between -50 to -100 N. (a) NMPTC. (b) IMPTC-1. (c) IMPTC-2.

A. Simulation Results

Based on the parameters given in Table III, simulations are conducted in the MATLAB/Simulink. First, the steady-state performance of the NMPTC method, proposed IMPTC-1 and IMPTC-2 methods are compared. Then, the dynamic performance of the three methods is also evaluated. Finally, the performance is tested for both flux-enhancing strategies CFE and DFE under both thrust variations.

A steady state performance comparison based on NMPTC method and the proposed IMPTC-12 methods is presented. The bus voltage is set to 100 V, while the peak thrust is configured at two different levels, corresponding to distinct steady-state conditions: bus voltage sufficiency operation and bus voltage insufficiency operation. The waveform comparison under the bus voltage-sufficient condition is presented in Fig. 15. As shown in the top row, each controller is capable of following the reference thrust under sufficient dc bus conditions. However, the thrust error under NMPTC is significantly larger compared to that of the proposed IMPTC methods, and it varies with the amplitude of the thrust. Since the dc-bus voltage is sufficient in this case, IMPTC-1 and IMPTC-2 exhibit nearly identical performance. The phase current waveforms also reveal that NMPTC exhibits significantly larger current ripple, despite all three methods maintaining similar overall current profiles. Notably, the maximum current variation in the IMPTC schemes is reduced by approximately 40% compared to that of NMPTC over the same time interval.

As the target thrust further increases, the fixed dc-bus voltage becomes insufficient to fully realize the commanded control voltage. Fig. 16 presents the corresponding thrust-tracking error, where the variable "Flag" indicates the modulation status. Flag $= 0$ means that the final reference VV remains inside the feasible hexagonal voltage region, whereas Flag $= 1$ denotes that the final reference vector reaches the hexagon boundary. The tracking error of NMPTC is more pronounced, exhibiting more intervals in which the modulation saturates. In contrast, IMPTC-1 and IMPTC-2 show a greater proportion of unsaturated modulation intervals, since the adopted optimal-vector selection strategy better adapts to varying thrust conditions. Moreover, benefiting from the reference-vector optimization scheme, IMPTC-2 achieves smaller thrust-tracking error than IMPTC-1 under the same voltage-constrained condition.

Under certain extreme sea conditions, the generator thrust may undergo sudden changes, which serve as an important indicator for evaluating the dynamic performance of the DDWEC control system. Fig. 17 illustrates the dynamic performance. The average response times of the three control strategies are 10.1, 5.65, and 4.25 ms, respectively. The results indicate that the adopted optimized VV selection strategy yields a marked enhancement in dynamic performance. Furthermore, by incorporating reference vector optimization into IMPTC-1, the proposed IMPTC-2 achieves improved control robustness against rapid variations in sea state conditions.

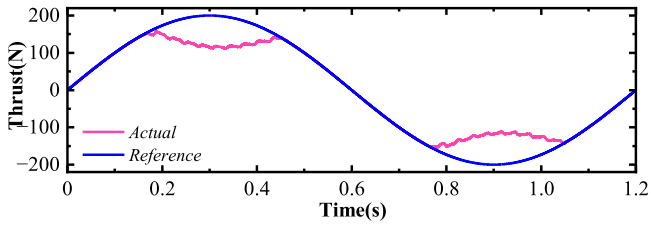

Fig. 18. Simulation results of thrust without flux-enhancing at a peak thrust of 200 N.

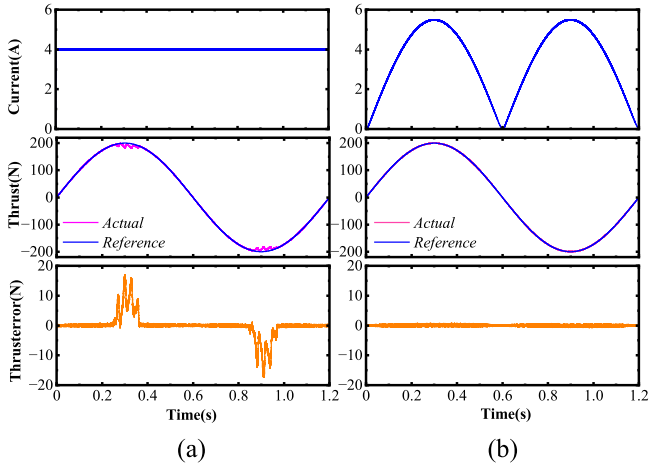

Fig. 19. Simulation results of field current and thrust at a peak thrust of 200 N. (a) Constant flux-enhancing. (b) Dynamic flux-enhancing.

When the peak thrust becomes excessively high, the resulting voltage demand may surpass the available bus voltage, thereby impeding accurate tracking of the reference thrust. As illustrated in Fig. 18, the observed clipping in the actual thrust waveform indicates that the system fails to deliver sufficient voltage, which is a direct manifestation of modulation saturation. Fig. 19 presents the results of two flux-enhancing strategies. As shown in Fig. 19(a), the excitation current is maintained at 4 A. Applying

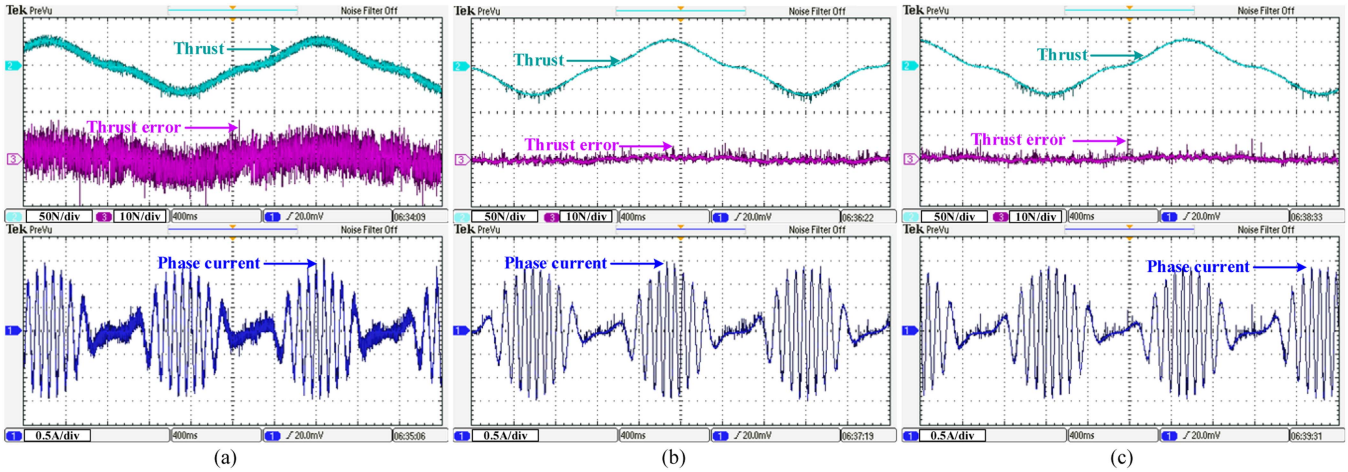

Fig. 20. Experimental results of thrust, thrust error and phase current at a peak thrust of 55 N. (a) NMPTC. (b) IMPTC-1. (c) IMPTC-2.

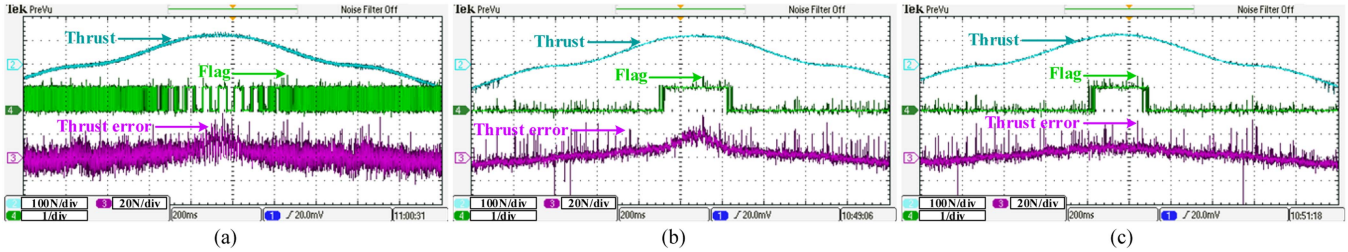

Fig. 21. Experimental results of thrust, thrust error and flag at a peak thrust of 120 N. (a) NMPTC. (b) IMPTC-1. (c) IMPTC-2.

a constant excitation field results in an increased peak thrust compared to operation without field current injection. However, when the generator operates under high electromagnetic thrust, significant fluctuations are observed at the peak thrust. These fluctuations can be mitigated through the DFE strategy, as illustrated in Fig. 19(b). In this strategy, the RMS value of the excitation current remains constant, while demonstrating improved dynamic performance.

B. Experimental Results

To further evaluate the control performance of the proposed strategy and to validate the simulation results. More experimental results are analyzed in this section base on experimental depicted platform in Fig. 14. The experimental thrust waveform exhibits a quasi-sinusoidal shape due to the kinematic characteristics of the crank–connecting rod mechanism. Moreover, the higher ripple level mainly arises from mechanical misalignment and converter switching effects.

1) *Steady-staTe Performance Comparison*: Fig. 20 presents the experimental waveforms of thrust, thrust error, and phase current under a low peak thrust condition for the three control strategies. As observed, all methods are capable of following the desired thrust trajectory. However, noticeable differences exist in the thrust tracking accuracy between NMPTC and IMPTCs. Compared to NMPTC, both IMPTC-1 and IMPTC-2 exhibit substantially reduced thrust error. The enhanced steady-state performance of the proposed method is further evidenced by the reduced current ripple and improved waveform smoothness. As shown from Fig. 11(a), the control vectors are frequently located on the boundary of the vector hexagon due to the inability of the bus voltage. Fig. 21 illustrates the experimental waveforms under elevated peak thrust conditions. Due to its vector selection strategy, NMPTC more frequently drives the control vectors to the boundary of the feasible region, resulting in reduced tracking accuracy—particularly under high thrust conditions. Although the proposed method may still encounter overmodulation, the optimal vector selection strategy adopted in IMPTCs effectively alleviates this issue. Besides, the reference vector optimization strategy adopted in IMPTC-2 enables further reduction of thrust error compared to IMPTC-1. Table V gives the steady-state thrust performance of the three control strategies under two operating conditions, including the maximum values $E_{\max}$ and root-mean-square (RMS) values RMS_{e} of the thrust tracking error

$$\mathrm{RMS}_e = \sqrt{\frac{1}{N}\sum_{i=1}^{N}\left[\frac{f_g^*(i)-f_g(i)}{f_g^*(i)}\right]^2} \times 100\%. \tag{47}$$

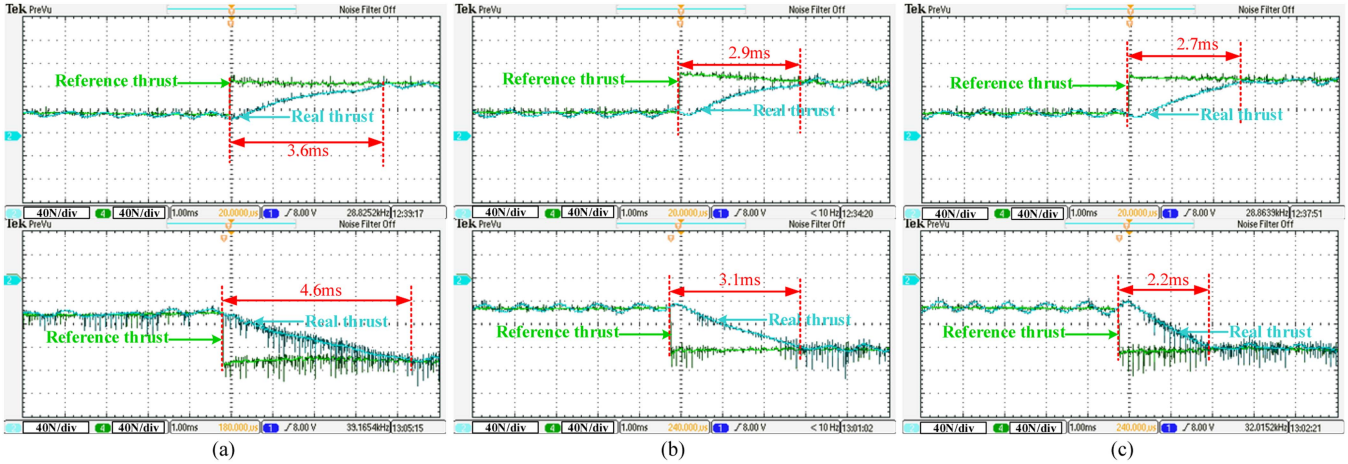

Fig. 22. Dynamic experimental results of three methods when the target thrust suddenly changes. (a) NMPTC. (b) IMPTC-1. (c) IMPTC-2.

TABLE V
STEADY-STATE PERFORMANCE UNDER THREE CONTROL METHODS

Conditions	Items	NMPTC	IMPTC-1	IMPTC-2
Low peak thrust	RMS_e	11.7%	4.1%	4.0%
	E_{max}	13.51 N	9.20 N	9.82 N
Large peak thrust	RMS_e	21.6%	11.2%	8.9%
	E_{max}	24.30 N	20.60 N	17.83 N

TABLE VI
DYNAMIC PERFORMANCE UNDER THREE CONTROL METHODS

Items	NMPTC	IMPTC-1	IMPTC-2
T_i	3.6 ms	2.9 ms	2.7 ms
T_d	4.6 ms	3.1 ms	2.2 ms

Under low peak thrust condition, compared with NMPTC, the RMS of thrust error with IMPTC is reduced over 7%, and the maximum thrust error is reduced over 25%. These experimental results demonstrate that the proposed IMPTC has obvious improvements in current quality and steady-state ripple compared with NMPTC under this condition. Although all methods experience performance degradation due to modulation constraints, IMPTC-2 maintains the lowest error metrics. Specifically, Compared with NMPTC and IMPTC-1, the RMS of thrust error with IMPTC-2 is reduced by 12.7% and 2.3%, respectively, and the maximum thrust error is reduced by 26.6% and 13.4%, respectively.

2) *Dynamic Performance Comparison*: Second, to assess system responsiveness under varying sea states, the transient performance of the three control strategies is evaluated. Fig. 22 illustrates the transient thrust response during abrupt changes in the reference value, including both a sudden increase and a sudden decrease. All three control strategies demonstrate a fast dynamic response, with the actual thrust closely tracking the reference signal. However, slight variations in response time are observed among the methods. As given in Table VI, the parameters T_i and T_d represent the response times for rising and falling thrust transitions. Compared with NMPTC and IMPTC-1, the torque ripple of IMPTC-2 is reduced by 28% and 18%, respectively.

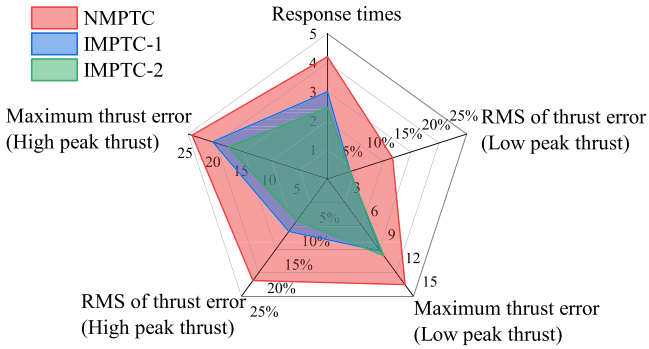

Fig. 23. Radar chart comparing the control performance of NMPTC, IMPTC-1, and IMPTC-2 under various evaluation metrics.

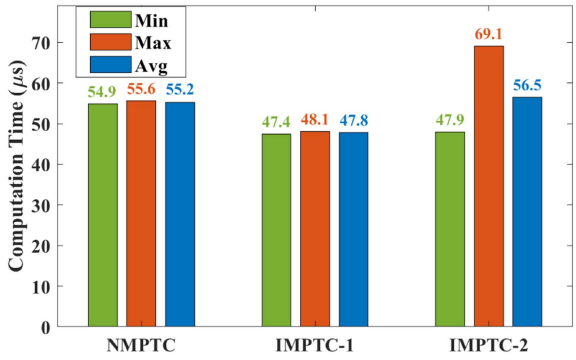

Fig. 24. Computation time of NMPTC, IMPTC-1, and IMPTC-2.

To facilitate a comprehensive comparison of the three control strategies under varying conditions, their performance across multiple evaluation metrics is summarized as Fig. 23. The proposed IMPTCs consistently outperforms NMPTC across

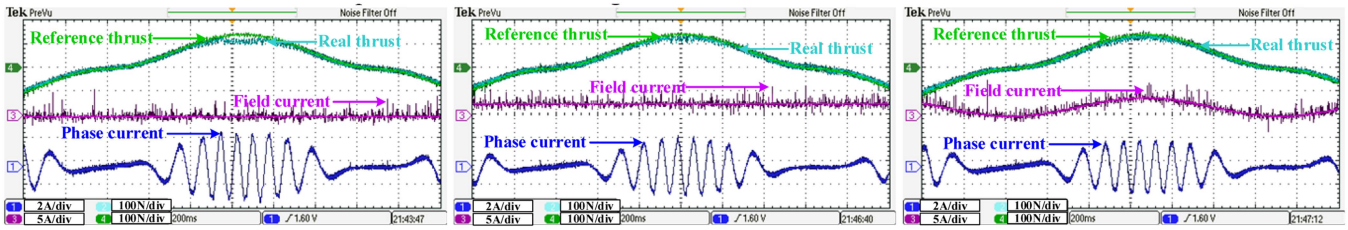

Fig. 25. Experimental results of reference thrust, real thrust, field current and phase current flag at a peak thrust of 140 N. (a) No field current. (b) Constant flux-enhancing. (c) Dynamic flux-enhancing.

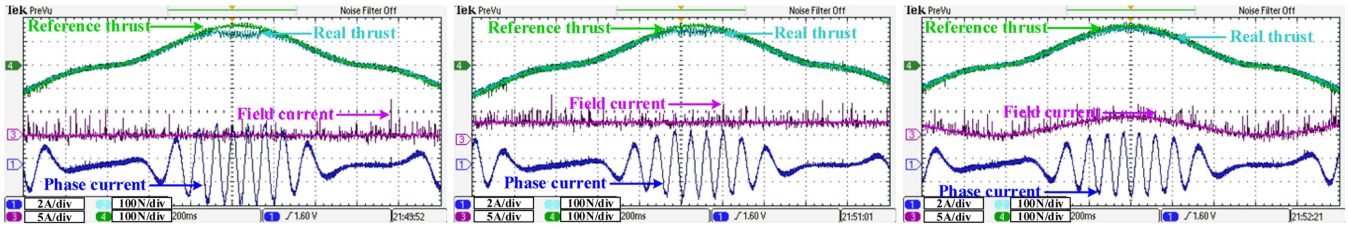

Fig. 26. Experimental results of reference thrust, real thrust, field current and phase current flag at a peak thrust of 170 N. (a) No field current. (b) Constant flux-enhancing. (c) Dynamic flux-enhancing.

all evaluated criteria, including the RMS and maximum thrust errors under low and high peak thrust conditions, as well as response time. For both IMPTC-1 and IMPTC-2, the steady-state performance is nearly identical under low peak thrust conditions. However, under high peak thrusts, IMPTC-2 demonstrates superior steady-state accuracy due to its reference vector optimization strategy. Consequently, IMPTC-1 demonstrates moderate improvement, while IMPTC-2 achieves the best overall performance with minimal thrust error and fastest dynamic response. Fig. 24 compares the computation times of the three predictive control strategies. It can be observed that the proposed IMPTC-1 achieves the lowest and most consistent computation time, indicating a reduced computational burden compared with the conventional NMPTC. Although IMPTC-2 exhibits a slightly higher maximum computation time owing to the additional overmodulation assessment and boundary-optimization step, its average execution time remains within the real-time constraint of the 100 μs sampling period. These results confirm that both IMPTC algorithms maintain computational feasibility for real-time implementation while providing enhanced thrust-tracking performance.

3) *Impacts of Different Flux-Enhancing Strategies:* Fig. 25 shows the experimental waveforms with different flux enhancing strategies. In Fig. 25(a), the field current is set to 0 A. When a peak thrust of 140 N is reached by the generator, the bus voltage of the system is already observed to struggle in supporting the increased electromagnetic force. Thus, thrust vibration is observed to be more pronounced at the peaks. To increase the peak thrust of the generator, the magnetic field must be enhanced by applying an excitation current. Therefore, significant jitter at the peak is eliminated under the two different flux-enhancing strategies, as illustrated in Fig. 25(b) and (c). As can be observed, the DFE yields a more pronounced improvement in force performance. As shown in Fig. 26, when the peak thrust is further increased to 170 N, the advantages of the proposed excitation strategy become more pronounced, demonstrating enhanced control capability under voltage constraints. The thrust tracking performance under different excitation strategies is given in Table VII. For a more intuitive comparison, the thrust error under different conditions is illustrated in Fig. 27. As the target thrust increases, the peak tracking deviation also grows. This degradation can be effectively mitigated through field enhancement. Furthermore, the applied DFE approach exhibits superior performance compared to CFE approach, achieving an average reduction of 43% in the maximum thrust error across the evaluated operating conditions.

TABLE VII
THRUST ERRORS WITH DIFFERENT FLUX-ENHANCING STRATEGIES

Items	Peak thrust of 140N		Peak thrust of 170N	
	RMS_e	E_{max}	RMS_e	E_{max}
No field current	11.4%	50N	14.1%	66N
CFE	9.7%	46N	11.6%	54N
DFE	8.6%	30N	9.2%	34N

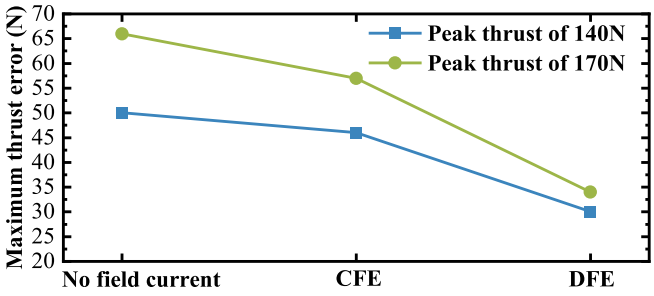

Fig. 27. Comparison of thrust errors with different flux-enhancing strategies.

It is worth noting that although the proposed method has been validated in the DDWEC system, the underlying control principle is general and can be extended to other electromechanical energy conversion platforms with similar dynamics.

VI. Conclusion

This article presented an improved MPTC with DFE for the HE-TF-PMLG in the DDWEC system. The suggest method enables the selection of an optimal control vector according to the thrust variation. The RMS of thrust error is reduced by over 7%, and the dynamic response time is shortened by approximately 28% relative to the baseline method. When the target thrust becomes excessively high, reference vector optimization is introduced to alleviate the overmodulation issue. Compared to MPTC-1, which does not incorporate reference vector optimization, MPTC-2 achieves a 2.3% reduction in thrust error and an 18% improvement in dynamic response time. A DFE strategy is developed to enhance the maximum thrust of the generator, demonstrating superior control performance under large wave conditions compared to traditional CFE method. The maximum thrust drop can be reduced by up to 43% under identical operating conditions. Both simulation and experimental results confirm that the proposed IMPTC strategy effectively enhances transient and steady-state thrust tracking performance, particularly under constrained dc bus voltage conditions.

References

[1] Z. Liao et al., "Modelling and control tank testing validation for attenuator type wave energy converter–Part II: Linear noncausal optimal control and deterministic sea wave prediction tank testing," *IEEE Trans. Sustain. Energy*, vol. 14, no. 3, pp. 1758–1768, Jul. 2023.

[2] Y. Zhang and G. Li, "Robust tube-based model predictive control for wave energy converters," *IEEE Trans. Sustain. Energy*, vol. 14, no. 1, pp. 65–74, Jan. 2023.

[3] A. S. Zurkinden, F. Ferri, S. Beatty, J. P. Kofoed, and M. M. Kramer, "Nonlinear numerical modeling and experimental testing of a point absorber wave energy converter," *Ocean Eng.*, vol. 78, pp. 11–21, 2014.

[4] A. F. D. O. Falcão, "Wave energy utilization: A review of the technologies," *Renew. Sustain. Energy Rev.*, vol. 14, no. 3, pp. 899–918, 2010.

[5] H. Polinder, B. C. Mecrow, A. G. Jack, P. G. Dickinson, and M. A. Mueller, "Conventional and TFPM linear generators for direct-drive wave energy conversion," *IEEE Trans. Energy Convers.*, vol. 20, no. 2, pp. 260–267, Jun. 2005.

[6] J. Zou, Q. Wang, and Y. Xu, "Influence of the permanent magnet magnetization length on the performance of a tubular transverse flux permanent magnet linear machine used for electromagnetic launch," *IEEE Trans. Plasma Sci.*, vol. 39, no. 1, pp. 241–246, Jan. 2011.

[7] M. A. Mueller, "Electrical generators for direct drive wave energy converters," *IEE Proc. - Gener., Transmiss. Distrib.*, vol. 149, no. 4, pp. 446–456, 2002.

[8] H. Polinder, M. E. C. Damen, and F. Gardner, "Linear PM generator system for wave energy conversion in the AWS," *IEEE Trans. Energy Convers.*, vol. 19, no. 3, pp. 583–589, Sep. 2004.

[9] M. Chen, L. Huang, Y. Li, G. Meng, and T. Xia, "A low thrust ripple flux-reversal transverse flux permanent magnet linear generator used in direct drive wave energy converter," *IEEE Trans. Magn.*, vol. 60, no. 9, Sep. 2024, Art. no. 8600505.

[10] J. V. Ringwood, G. Bacelli, and F. Fusco, "Energy-maximizing control of wave-energy converters: The development of control system technology to optimize their operation," *IEEE Control Syst. Mag.*, vol. 34, no. 5, pp. 30–55, Oct. 2014.

[11] F. Fusco and J. V. Ringwood, "A simple and effective real-time controller for wave energy converters," *IEEE Trans. Sustain. Energy*, vol. 4, no. 1, pp. 21–30, Jan. 2013.

[12] J. Na, B. Wang, G. Li, S. Zhan, and W. He, "Nonlinear constrained optimal control of wave energy converters with adaptive dynamic programming," *IEEE Trans. Ind. Electron.*, vol. 66, no. 10, pp. 7904–7915, Oct. 2019.

[13] S. Zhan, G. Li, and C. Bailey, "Economic feedback model predictive control of wave energy converters," *IEEE Trans. Ind. Electron.*, vol. 67, no. 5, pp. 3932–3943, May 2020.

[14] Z. Lin, J. Wang, and D. Howe, "A learning feed-forward current controller for linear reciprocating vapor compressors," *IEEE Trans. Ind. Electron.*, vol. 58, no. 8, pp. 3383–3390, Aug. 2011.

[15] M. A. M. Cheema, J. E. Fletcher, D. Xiao, and M. F. Rahman, "A direct thrust control scheme for linear permanent magnet synchronous motor based on online duty ratio control," *IEEE Trans. Power Electron.*, vol. 31, no. 6, pp. 4416–4428, Jun. 2016.

[16] R. Cao and K. S. Low, "A repetitive model predictive control approach for precision tracking of a linear motion system," *IEEE Trans. Ind. Electron.*, vol. 56, no. 6, pp. 1955–1962, Jun. 2009.

[17] J. Ji, R. Xue, W. Zhao, T. Tao, and L. Huang, "Simplified three-vector-based model predictive thrust force control with cascaded optimization process for a double-side linear vernier permanent magnet motor," *IEEE Trans. Power Electron.*, vol. 35, no. 10, pp. 10681–10689, Oct. 2020.

[18] X. Sun, M. Wu, C. Yin, and S. Wang, "Model predictive thrust force control for linear motor actuator used in active suspension," *IEEE Trans. Energy Convers.*, vol. 36, no. 4, pp. 3063–3072, Dec. 2021.

[19] S. A. Davari, D. A. Khaburi, and R. Kennel, "An improved FCS–MPC algorithm for an induction motor with an imposed optimized weighting factor," *IEEE Trans. Power Electron.*, vol. 27, no. 3, pp. 1540–1551, Mar. 2012.

[20] L. Tang et al., "Model predictive thrust control for linear induction machine: A fuzzy optimization approach," *IEEE Trans. Ind. Appl.*, vol. 59, no. 2, pp. 2532–2545, Mar./Apr. 2023.

[21] M. F. Elmorshedy, W. Xu, S. M. Allam, J. Rodriguez, and C. Garcia, "MTPA-based finite-set model predictive control without weighting factors for linear induction machine," *IEEE Trans. Ind. Electron.*, vol. 68, no. 3, pp. 2034–2047, Mar. 2021.

[22] W. Huang, W. Hua, F. Yin, F. Yu, and J. Qi, "Model predictive thrust force control of a linear flux-switching permanent magnet machine with voltage vectors selection and synthesis," *IEEE Trans. Ind. Electron.*, vol. 66, no. 6, pp. 4956–4967, Jun. 2019.

[23] Z. Liu et al., "A modified deadbeat predictive current control for improving dynamic performance of PMSM," *IEEE Trans. Power Electron.*, vol. 37, no. 12, pp. 14173–14185, Dec. 2022.

[24] Z. Jin, W. Xu, J. Wang, and T. Xu, "Dynamic current trajectory tracking strategy with optimized overmodulation method for permanent magnet synchronous motor drives," *IEEE Trans. Ind. Appl.*, vol. 60, no. 6, pp. 8867–8877, Nov./Dec. 2024.

[25] A. Sarajian et al., "Overmodulation methods for modulated model predictive control and space vector modulation," *IEEE Trans. Power Electron.*, vol. 36, no. 4, pp. 4549–4559, Apr. 2021.

[26] C. F. Garcia, C. A. Silva, J. R. Rodriguez, P. Zanchetta, and S. A. Odhano, "Modulated model-predictive control with optimized overmodulation," *IEEE J. Emerg. Sel. Top. Power Electron.*, vol. 7, no. 1, pp. 404–413, Mar. 2019.

[27] S. Zhan, J. Na, and G. Li, "Nonlinear noncausal optimal control of wave energy converters via approximate dynamic programming," *IEEE Trans. Ind. Informat.*, vol. 15, no. 11, pp. 6070–6079, Nov. 2019.

[28] D. García-Violini, Y. Peña-Sanchez, N. Faedo, F. Ferri, and J. V. Ringwood, "A broadband time-varying energy maximising control for wave energy systems (LiTe-Con+): Framework and experimental assessment," *IEEE Trans. Sustain. Energy*, vol. 14, no. 3, pp. 1516–1525, Jul. 2023.

[29] H. A. Said, D. García-Violini, and J. V. Ringwood, "Wave-to-grid (W2G) control of a wave energy converter," *Energy Convers. Manage., X*, vol. 14, 2022, Art. no. 100190.

Jianlong Yang (Student Member, IEEE) was born in Jiangxi, China, in 2000. He received the B.S. degree in electrical engineering and automation from Harbin University of Science and Technology, Harbin, China, in 2021. He is currently working toward the Ph.D. degree with the Southeast University, Nanjing, China. His research interests include the wave energy system control and permanent magnet linear generator control.

Lei Huang (Member, IEEE) received the B.Eng. and M.Eng. degrees from the China University of Petroleum, Dongying, China, in 2002 and 2008, respectively, and the Ph.D. degree from the Southeast University, Nanjing, China, in 2012, all in electrical engineering. He is currently an Associate Professor in electrical engineering with the Southeast University, Nanjing, China. He was a Visiting Scholar with the University of Sheffield, Sheffield, U.K., from 2017 to 2018. His research interests include linear generators and electromechanical energy conversion to direct-drive wave energy conversion.

Hui Yang (Senior Member, IEEE) received the B. Eng. degree from Dalian University of Technology, Dalian, China, in 2011, and the Ph.D. degree from Southeast University, Nanjing, China, in 2016, respectively, all in electrical engineering. From 2014 to 2015, he was supported by the China Scholarship Council through a one-year joint Ph.D. studentship at The University of Sheffield, Sheffield, U.K. From 2019 to 2020, he was a Postdoctoral Fellow with School of Electrical Engineering, The Hong Kong Polytechnic University. From 2016 to 2024, he was with Southeast University, China, and he is currently a Full Professor at the College of Automation Engineering, Nanjing University of Aeronautics and Astronautics. He has authored or co-authored more than 120 IEEE Transactions papers and is the holder of more than 40 patents in these areas. His research interests include novel permanent-magnet machines and drives with particular reference to variable-flux machines for electric vehicles, robotics, and renewable energy applications. Dr. Yang is currently an Associate Editor for IEEE TRANSACTIONS ON INDUSTRIAL ELECTRONICS, IEEE TRANSACTIONS ON ENERGY CONVERSION, and an Editor of WEVJ. He was the Organizing Committee Chair of iSPEC 2021 and CIEEC 2022.

Minshuo Chen (Member, IEEE) was born in Ganzhou, China. He received the B.Eng. degree in electrical power systems and automation from North China Electric Power University, Baoding, China, in 2014, and the M.Eng. and Ph.D. degrees from Southeast University, Nanjing, China, in 2018 and 2024, respectively, both in electrical engineering. He is currently a Lecturer with the School of Electric Power Engineering, Nanjing Institute of Technology, Nanjing, China. He is also involved in the work at the Advanced Ocean Institute of Southeast University, Nantong, China. He has been engaged in post-doctoral research work at Jiangsu University on a part-time basis since 2025. His research interests include linear machine, wave energy converter, and transverse flux machine